Search of low-mass WIMPs with a *p*-type point contact germanium detector in the CDEX-1 experiment

W. Zhao,[1] Q. Yue,[1,*] K. J. Kang,[1] J. P. Cheng,[1] Y. J. Li,[1] H. T. Wong,[7,†] S. T. Lin,[2,7,‡] J. P. Chang,[5] J. H. Chen,[7,†] Q. H. Chen,[1] Y. H. Chen,[6] Z. Deng,[1] Q. Du,[4] H. Gong,[1] X. Q. Hao,[1] H. J. He,[1] Q. J. He,[1] H. X. Huang,[3] T. R. Huang,[7,†] H. Jiang,[1] H. B. Li,[7,†] J. Li,[1] J. Li,[5] J. M. Li,[1] X. Li,[3] X. Y. Li,[4] Y. L. Li,[1] F. K. Lin,[7,†] S. K. Liu,[2] L. C. Lü,[1] H. Ma,[1] J. L. Ma,[1] S. J. Mao,[5] J. Q. Qin,[1] J. Ren,[3] J. Ren,[1] X. C. Ruan,[3] V. Sharma,[7,8] M. B. Shen,[6] L. Singh,[7,8,†] M. K. Singh,[7,†] A. K. Soma,[7,†] J. Su,[1] C. J. Tang,[2] J. M. Wang,[6] L. Wang,[1] Q. Wang,[1] S. Y. Wu,[6] Y. C. Wu,[5] Z. Z. Xianyu,[1] R. Q. Xiao,[1] H. Y. Xing,[2] F. Z. Xu,[1] Y. Xu,[4] X. J. Xu,[1] T. Xue,[1] L. T. Yang,[1] S. W. Yang,[7,†] N. Yi,[1] C. X. Yu,[4] H. Yu,[1] X. Z. Yu,[2] M. Zeng,[1] X. H. Zeng,[6] Z. Zeng,[1] L. Zhang,[5] Y. H. Zhang,[6] M. G. Zhao,[4] Z. Y. Zhou,[3] J. J. Zhu,[2] W. B. Zhu,[5] X. Z. Zhu,[1] and Z. H. Zhu[6]

(CDEX Collaboration)

[1]*Key Laboratory of Particle and Radiation Imaging (Ministry of Education) and Department of Engineering Physics, Tsinghua University, Beijing 100084*
[2]*College of Physical Science and Technology, Sichuan University, Chengdu 610064*
[3]*Department of Nuclear Physics, China Institute of Atomic Energy, Beijing 102413*
[4]*School of Physics, Nankai University, Tianjin 300071*
[5]*NUCTECH Company, Beijing 10084*
[6]*YaLong River Hydropower Development Company, Chengdu 610051*
[7]*Institute of Physics, Academia Sinica, Taipei 11529*
[8]*Department of Physics, Banaras Hindu University, Varanasi 221005*

(Received 19 January 2016; published 6 May 2016)

The CDEX-1 experiment conducted a search of low-mass (< 10 GeV/c^2) weakly interacting massive particles dark matter at the China Jinping Underground Laboratory using a p-type point-contact germanium detector with a fiducial mass of 915 g at a physics analysis threshold of 475 eVee. We report the hardware setup, detector characterization, data acquisition, and analysis procedures of this experiment. No excess of unidentified events is observed after the subtraction of the known background. Using 335.6 kg-days of data, exclusion constraints on the weakly interacting massive particle-nucleon spin-independent and spin-dependent couplings are derived.

DOI: 10.1103/PhysRevD.93.092003

I. INTRODUCTION

The long-term goal of the China Dark Matter Experiment (CDEX) program [1] is to conduct an experiment at the China Jinping Underground Laboratory (CJPL) [2] with a ton-scale point-contact germanium detector array for low-mass weakly interacting massive particle (WIMP) searches [3–5] and studies of double-beta decay in ^{76}Ge [3,5–7].

The pilot experiment CDEX-0 was with small planar germanium detectors in array form with a target mass of 20 g [8], achieving a threshold of 177 eVee (electron equivalent energy eVee is used to characterize detector response throughout in this article, unless otherwise stated). The CDEX-1 experiment adopted kg-scale p-type point-contact germanium (pPCGe) detectors [9,10]. Data taking of the first phase was performed only with a passive shielding system, and dark matter results were published with 14.6 kg-days of data taken from August to September 2012 and a threshold of 400 eVee [10]. Starting November 2013, Phase-II measurements were based on the design of earlier work [8,11], with an active NaI(Tl) anti-Compton (NaI-AC) detector installed. First results with 53.9 kg-days of data were reported [12], providing an order of magnitude improvement on the spin-independent χ-N coupling (WIMPs denoted by χ). In particular, the allowed region implied by the CoGeNT [13] experiment is probed and excluded with an identical detector target.

We describe the details of the CDEX-1 experiment and report the results with 335.6 kg-days of data taking at CJPL in the following sections.

II. EXPERIMENTAL SETUP

A. China Jinping Underground Laboratory

The China Jinping Underground Laboratory is located in the Sichuan province, with a vertical rock overburden of more than 2400 m, providing 6720 m of water equivalent

*Corresponding author.
yueq@mail.tsinghua.edu.cn
†Participating as a member of TEXONO Collaboration.
‡Corresponding author.
linst@phys.sinica.edu.tw

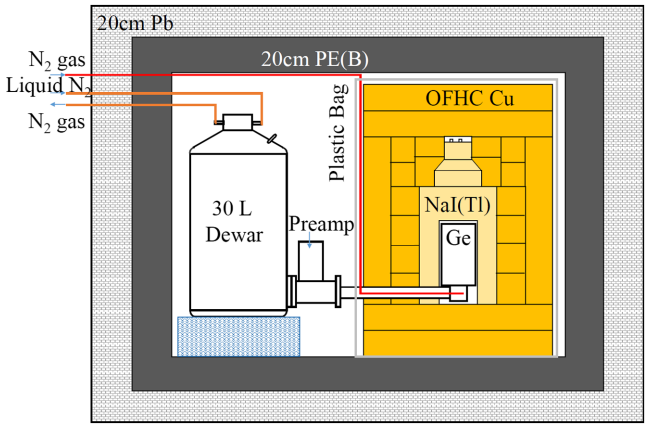

FIG. 1. Schematic diagram of the CDEX-1 experimental setup; the "Ge" represents the germanium crystal of the 1 kg *p*PCGe.

overburden as a passive shield against cosmic rays and their induced backgrounds. The flux of cosmic ray and associated backgrounds is down to 61.7 $y^{-1} \cdot m^{-2}$ [14]. In addition, the radioactivities of ^{232}Th, ^{238}U, and ^{40}K from rock surrounding CJPL were very low based on *in situ* measurement. The low cosmic-ray flux and radioactivities of ^{238}U and ^{232}Th gave rise to a low level of neutron flux. The measured ambient fast and thermal neutron fluxes are 1.5×10^{-7} [15] and 4.00×10^{-6} $cm^{-2}\,s^{-1}$ [16], respectively. The ambient gamma radioactivity gives a background rate of 3.94×10^{3} $kg^{-1}\,keV^{-1}\,day^{-1}$ to an unshielded germanium detector at the energy range of 40–2700 keV [17].

B. Detector hardware

The CDEX-1 experiment adopted one single module at 1 kg-scale mass *p*PCGe to search for WIMPs. The p-type germanium crystal is a cylinder with about 62 mm of both height and diameter which give rise to 994 g of mass. It has two electrodes: the outer electrode is n^+ type, providing high voltage (HV) and signal, and the tiny pointlike center electrode is p^+ type, with order of 1 mm diameter. This gives rise to the order of 1 pF capacitance which, in principle, would contribute to the low-energy threshold. At the Phase-I experiment, the outer electrode signal was read out by a resistive feedback preamplifier [10]. At the Phase-II measurement, the signal output was removed due to its induced noise, such that the outer electrode served only as a HV electrode. The center electrode signal was read out by an ultralow noise junction field-effect transistor (JFET) nearby and then supplied into a pulsed-reset feedback preamplifier. The preamplifier generated three identical energy-related signals (OUT_E), one timing-related signal (OUT_T) and one inhibit signal (IHB) marking the inactive time of the preamplifier. Meanwhile, the preamplifier can accept a test input, typically from an electronic pulser to simulate physical signals.

The NaI(Tl) scintillator crystal of the anti-Compton (AC) detector is well shaped and can enclose the cryostat of the *p*PCGe, as shown in Fig. 1, and the thicknesses of its side and top are 48 and 130 mm, respectively. The scintillation light from the NaI(Tl) crystal was read out by a photomultiplier tube, which has two outputs from an anode and dynode, respectively; one was loaded to a shaping amplifier (SA) at high gain determining the time over the NaI-AC energy threshold, and another was loaded to a timing amplifier (TA) at low gain, which was used to measure energy as well as discriminate background sources based on pulse characteristics for different radiation.

The schematic of the CDEX-1 data acquisition (DAQ) system is shown in Fig. 2 and was based on commercial

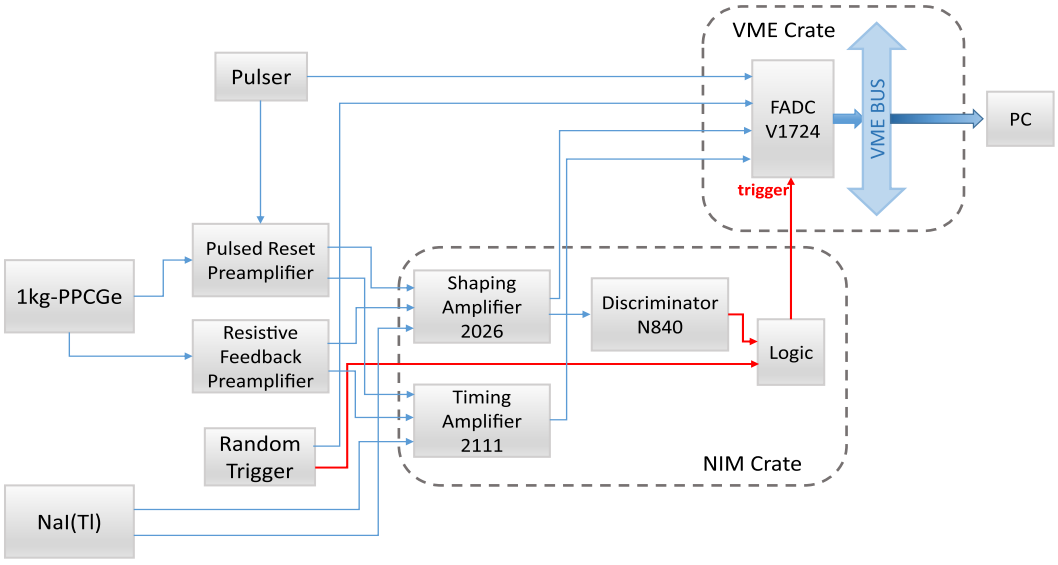

FIG. 2. Schematic diagram of the data acquisition system for CDEX-1 Phase II.

NIM/VME modules and crates from CANBERRA and CAEN. The pPCGe worked at +3500 V provided by a high voltage module (CANBERRA 3106D). The three identical OUT_E signals were loaded to shaping amplifiers (CANBERRA 2026) at 6 μs (S_{p6}), 12 μs shaping time (S_{p12}), and a timing amplifier (CANBERRA 2111) (T_p), respectively. Each gain of these amplifiers was adjusted to achieve the maximal signal-to-noise ratio and maximal information for low-energy events. The dynamic range was limited to 12 keVee due to the saturation of the shaping amplifier. The $S_{p6,12}$ signal provided the energy measurement and system trigger of the DAQ. The T_p signal recorded the raw pulse shape information of one event, so it was able to provide the rise time information. The OUT_T signal was distributed into a timing amplifier with low gain to measure high-energy backgrounds, intending to analysis the background source and opening a window to study ^{76}Ge neutrinoless double-beta decay. These outputs were digitized and recorded by a flash analog-to-digital convertor (FADC, CAEN V1724) at a 100 MHz sampling rate with a resolution of 14 bits. The data acquisition software is based on the LabVIEW program. The discriminator output of the inhibit signal provided another trigger of the DAQ and was recorded to determine the exact time of the beginning of discharge process of the preamplifier. To monitor the noise level and dead time of the system, random trigger signals (RT) at 0.05 Hz generated by a precision pulser were injected into the system, providing the system trigger.

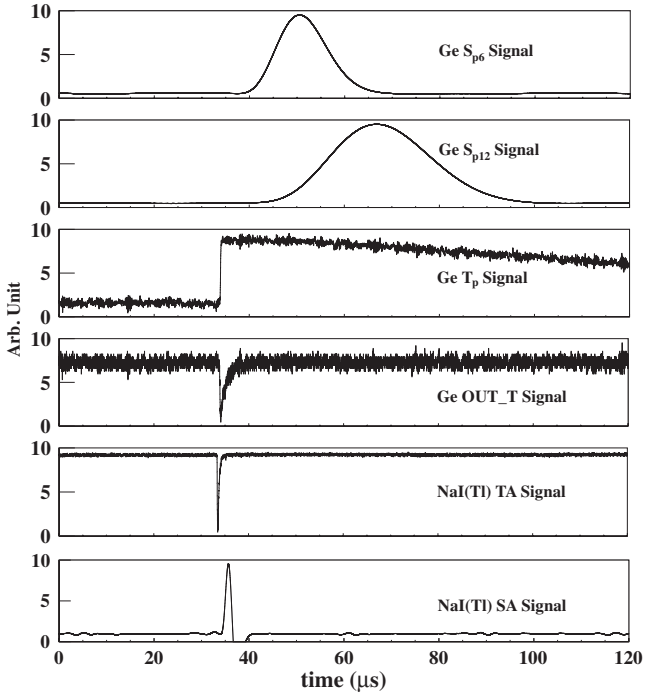

FIG. 3. Example of one AC^+ event recorded by FADC, corresponding to energy ~10.37 keVee deposited in pPCGe.

The NaI-AC detector was optimized on its energy threshold, energy linearity in the broad energy range, energy resolution, and stability. The NaI-AC signals were recorded only when the pPCGe detector was fired and triggered the DAQ, and this kind of coincidence event was denoted as AC^+. The anticoincidence events, which only fired in the pPCGe detector but without signals at the NaI-AC detector, were denoted as AC^-. Figure 3 shows an example of an AC^+ event recorded by the DAQ. In general, the DAQ took data at a low trigger rate (~3–5 Hz) to decrease the penalty of dead time.

C. Shielding system

The passive shielding structure of CDEX-1 in CJPL is displayed in Fig. 1. The outermost is 20 cm of lead to shield ambient gamma rays. The inner is a 20 cm thick layer of ~30% borated polyethylene, acting as a thermal neutron absorber. At the Phase-I experiment, the innermost is a minimum of 20 cm of oxygen free high conductivity (OFHC) copper which encloses the detector cryostat in all directions and further reduces residual gamma rays surviving the outer shields. Exterior to the OFHC shield is a plastic bag, which is used to seal the working space to prevent radon incursion. The radon exclusion volume is continuously flushed with nitrogen gas from a pressurized Dewar. At the Phase-II experiment, interior to OFHC shield is a NaI-AC detector with a well-shaped cavity enclosing the pPCGe detector cryostat to provide passive and active shielding. A detailed discussion about its performances is provided in Sec. III. The entire structure was located in a room with 1 m thick polyethylene walls, which can moderate and absorb ambient neutrons. Based on complete simulations, the shielding structure can attenuate ambient gamma and neutron fluxes by factors of $>10^{12}$ [18] and $>10^{13}$ [19], respectively.

III. DETECTOR CHARACTERIZATION

The performances of the detection system were studied in detail. Characterization of the pPCGe, the NaI-AC, and the DAQ are discussed in the following sections.

A. Energy definition and calibration

A typical pulse of the pPCGe was displayed in Fig. 4, with the parameters defined consistently for all channels. Two energy-related parameters are defined: (i) the maximal amplitude of one pulse (A_{max}) and (ii) the integration of one pulse (Q). The Q of S_{p6} was chosen to define as energy (E) for its excellent energy linearity at the low-energy range. Since the active volume of pPCGe crystal is surrounded by a ~1.0 mm dead layer and 1.5 mm of OFHC copper cryostat, external low-energy x rays at the <50 keVee range cannot penetrate into the active volume of the pPCGe crystal. Energy calibration was therefore done with its internal characteristic x rays originating from the electron

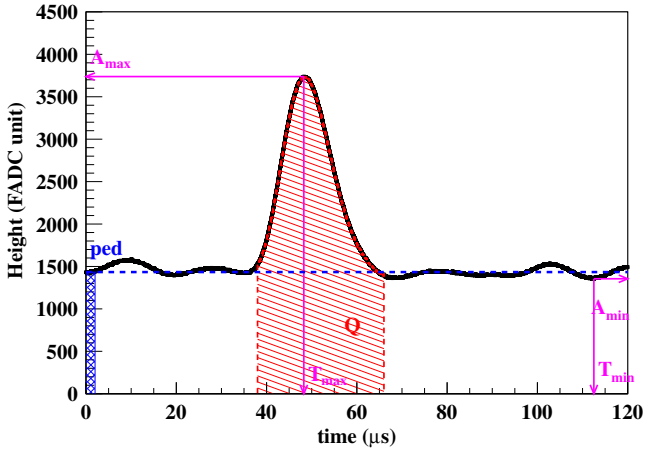

FIG. 4. Typical pulse of S_{p6} at 1.84 keVee. Some parameters are defined: (A_{max}, T_{max}) represent the maximal amplitude and its corresponding time of the pulse; (A_{min}, T_{min}) represent the minimal amplitude and its corresponding time of the pulse; Q corresponds to the integral of the pulse; and Ped means the pedestal of the pulse.

capture of the cosmogenic radioisotopes [10,12,20]. Figure 5(a) shows the energy calibration by the two dominant K-shell x rays: ^{68}Ge (10.368 keVee), ^{65}Zn (8.98 keVee), and RT events (0 keVee). The inset figure displays the energy difference between the calibrated energy and the real energy of these three peaks, together with other peaks observed in the measured CDEX-1 background spectrum, demonstrating good linearity of less than 0.8% deviation. The relationship between energy and its resolution is also depicted in Fig. 5(b), showing good linearity between $\sqrt{E}$ and the energy resolution full width at half maximum. The energy resolution in the low-energy region is derived from this line.

The NaI-AC detector was developed with an emphasis on low-energy threshold to achieve high efficiency of AC$^+$ background suppression. A_{max} was used to define its energy and was calibrated by a ^{152}Eu (121.78, 244.70, 344.28 keV) source together with RT events. The energy threshold of the NaI-AC detector achieved was as low as 6 keVee for background measurement, as illustrated in Fig. 6.

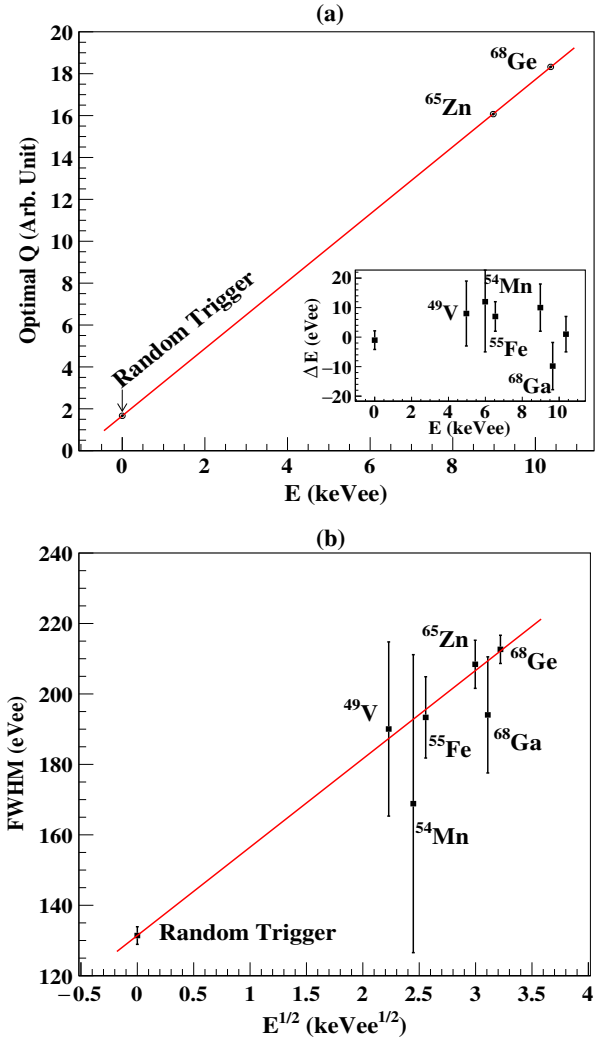

FIG. 5. (a) Calibration line relating the optimal Q measurements from S_{p6} with the known energies from ^{68}Ge and ^{65}Zn K-shell x rays and RT. The error bars are smaller than the data point size. The energy difference between the energy derived from the calibration and the real energy for these three peaks is depicted in the inset, together with K-shell x rays of ^{68}Ga, ^{55}Fe, ^{54}Mn, and ^{49}V. (b) Relation between the energy of K-shell x rays and energy resolution.

B. Quenching factor

The quenching factor (QF) is defined as the ratio of the measured energy to the total nuclear recoil energy deposited in the detector medium. It is crucial to know the relation between the QF and nuclear recoil energy in the studies of the WIMP search. Figure 7 shows a compilation of all experiment measurements and calculations of the QF for recoiled germanium nuclei [12]. Several experiments have measured the QF down to a few keVnr (nuclear recoil energy). Typically, two methods can be used to calculate the QF for different nuclear recoil energy. In TRIM software simulation, several aspects of the stopping power, range, and straggling distributions of a recoiled nucleon with certain energy are considered, while Hartree-Fock atoms and lattice effects are also included [21]. In analytic Lindhard calculation, an ideal and static atom is adopted, and the Lindhard model is parametrized to a constant k which is related to the stopping power [22]. The TRIM results agree well with the QF experimental results at a larger energy range and therefore are adopted in our analysis. As illustrated in Fig. 7, the QF function derived from TRIM with a 10% systematic uncertainty is applied in our analysis.

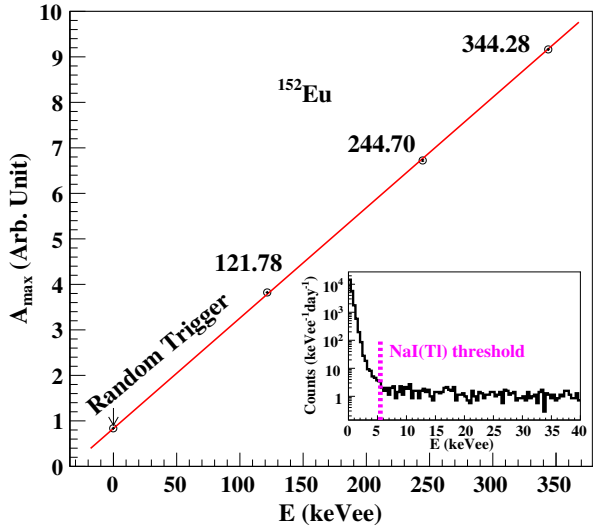

FIG. 6. Energy calibration for the NaI(Tl) SA channel. The error bars are smaller than the data point size. The inset figure depicts the measured background energy spectrum of NaI(Tl), and the energy threshold was set at the edge of noise.

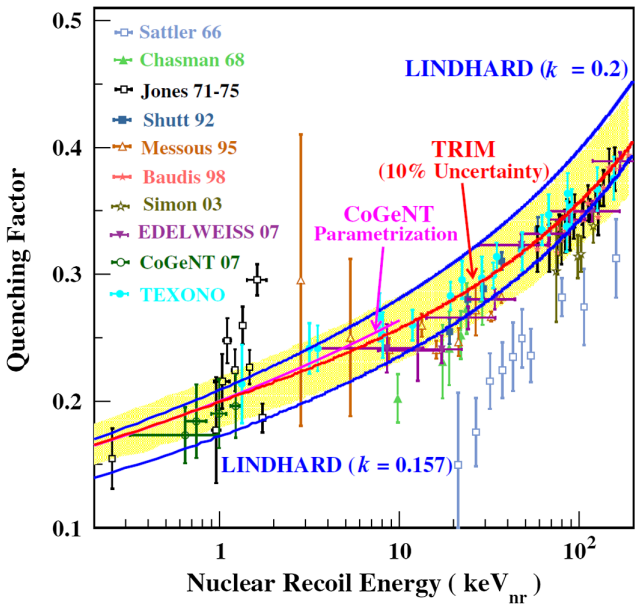

FIG. 7. QF results for germanium from both experiments and calculations. The QF curve which is derived from TRIM [21] as a function of nuclear recoil energy, together with a 10% systematic error band. The various experimental measurements are overlaid, so are the alternative QFs from the parametrization of CoGeNT [13] and the Lindhard theory [22] at $k = 0.2$ and $k = 0.157$ adopted by CDMSlite [23]. It shows that the TRIM results with uncertainties cover most data points as well as the alternative formulations.

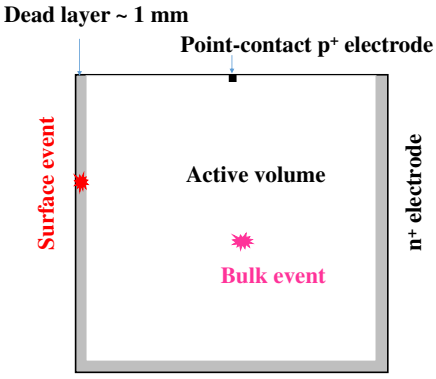

FIG. 8. Schematic diagram of pPCGe crystal configuration.

C. Dead layer

The n^+ outer surface electrode of pPCGe is fabricated by lithium diffusion, resulting in normally about 1 mm depth of the dead layer. This dead layer is composed of a totally dead layer where the electric field is zero and a transition layer where the electric field is weak. The interior of the transition layer is the active volume. Electron-hole pairs generated from events taking place in the transition layer have slower drift velocity than those in active volume, leading to a pulse with a typically slow rise time as well as degraded amplitude due to partial charge collection [24]. We denoted events at the active volume with complete charge collection as bulk events and events at the dead layer as surface events, as illustrated in Fig. 8. The totally dead layer acted as a passive shield against external low-energy γ/β, and the transition layer actds as an active shield against ambient gamma rays through bulk/surface events discrimination based on rise time characteristics. This was the self-shield effect of pPCGe. On the contrary, the dead layer produced fiducial mass loss. Since the attenuation of gamma rays by the dead layer was dependent on energy, the ratio of the intensities of these gamma rays at photo-electron peaks were be different from the original one. The ^{133}Ba source with various energy gamma rays was used to measure the thickness of the dead layer for the pPCGe, and it was derived as (1.02 ± 0.14) mm via the comparison of measured and simulated intensity ratios of those gamma peaks [25,26]. This gave rise to the fiducial mass as 915 g with 1% uncertainty.

D. Trigger efficiency

In principle, physical events over the DAQ threshold would produce triggers and be recorded. The efficiency that events produced triggers for the DAQ is defined as the trigger efficiency, which was 50% for events at the discriminator threshold. AC^+ events from the source sample were used to derive the trigger efficiency [8,10,27]. Figure 9 displays the trigger efficiency together with the 1σ band derived from the ^{137}Cs AC^+ sample. It is shown that the trigger threshold was 246 ± 2 eVee, and the

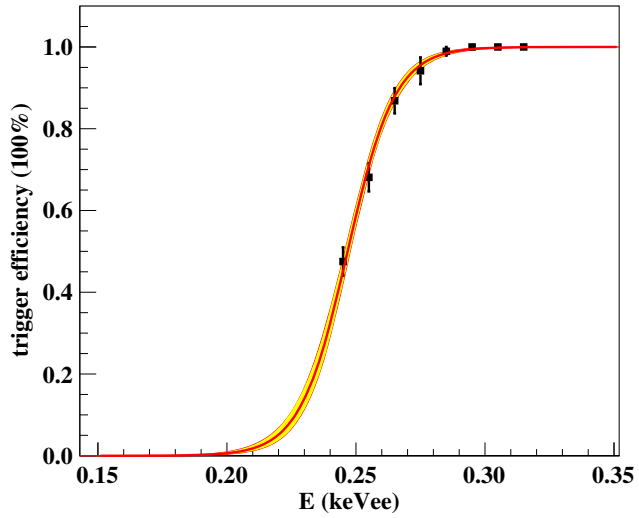

FIG. 9. Trigger efficiency derived from ^{137}Cs AC^{+} samples, adopting the error function to fit the experiment data points and with a $1\,\sigma$ band of the error superimposed.

trigger efficiency was 100% above our analysis threshold 475 eVee.

E. Stability

Both the trigger rate and the noise of RT of the *p*PCGe detector were monitored, shown in Fig. 10. An improvement of the laboratory power supply took place at the time period of I. A power filter was used to stabilize the power supply, and the electronic noise of the detector system decreased around 10%. Calibration was performed from late July to late August 2014, corresponding to the time period of II. During the time period of III and IV, the construction work at the polyethylene (PE) room prevented data taking. Both the trigger rate and the noise of RT were kept stable to 16% and 2%, respectively, during the data taking periods.

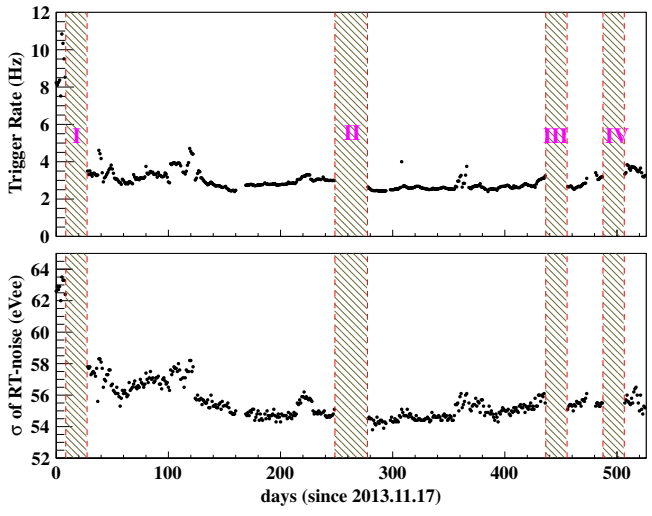

FIG. 10. Top panel: daily average trigger rate of the *p*PCGe detector system. Bottom panel: daily average RT electronic noise of the *p*PCGe detector system.

IV. DATA ANALYSIS

The data analysis is based on timing and amplitude parameters extracted from pulses recorded by the DAQ described in Sec. II.B.

A. Parameters definition

The amplitude parameters are defined in Sec. III.A. The timing parameters can be classified into three categories: (i) the timing differences between one event and its closest prior and post IHB events, denoted as T_{-} and T_{+}, the detailed information of which is described in Ref. [10]; (ii) the timing interval of one event recorded by the *p*PCGe detector and the NaI-AC detector, Δt; and (iii) the rise time of one event τ, defined as the time interval between 5% and 95% of the T_p pulse height. To calculate the τ, the pulse-processing algorithm in Refs. [12,20,24] was applied. This rise-time provides the location information where one event happened, in active volume or in the dead layer, to discriminate the bulk/surface events.

B. Data selection

We developed one data selection procedure to determine the WIMP-induced nuclear recoil events, after the data set calibration and data quality checking [10]. The procedure contains three categories of selection criteria:

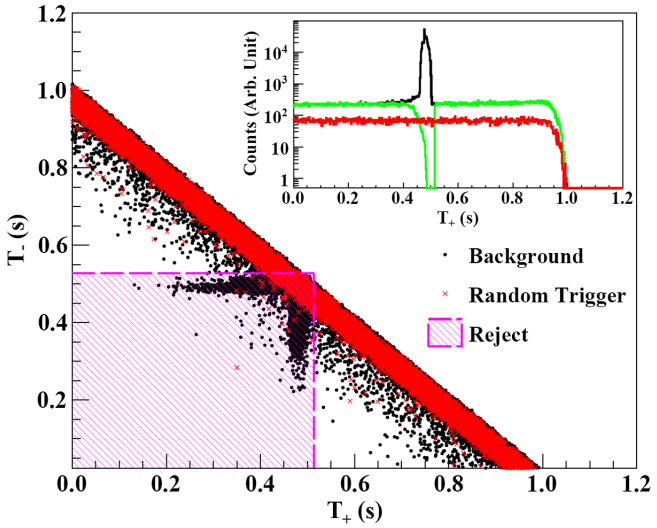

FIG. 11. The scatter plots of T_{-} and T_{+} for random trigger events and background events. The TT cut has also been overlain on the scatter plot. The inset figure shows the T_{+} spectra of background before (black) and after the TT cut (green), together with the T_{+} spectra for RT events (red).

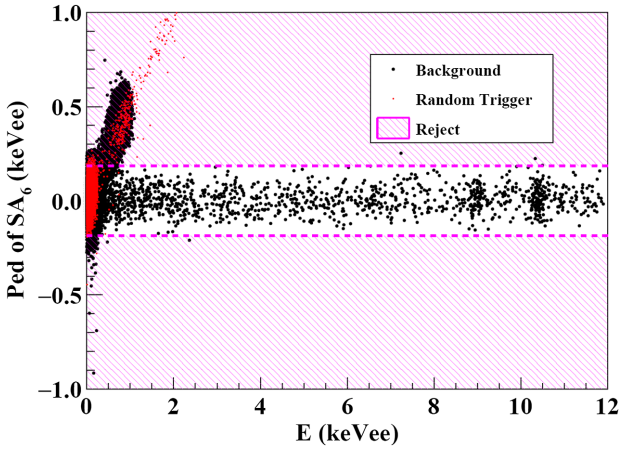

FIG. 12. The distributions of Ped of S_{p6} for both background and RT events and of the Ped cut criteria.

(1) Basic cuts (BCs): These basic criteria were aimed to differentiate physical events from electronic noise and spurious signals, such as microphonics. Several methods were applied to eliminate noise events according to their characteristics. The first method was based on the timing information of events, derived from the distribution of parameters T_- and T_+, and the class of midperiod noise with obvious timing distinction was identified and wiped out by the TT cut as shown in Fig. 11. The second method was deduced from the pedestal of $S_{p6,12}$ and T_p (Ped), which was irrelevant to the pulse shape, and therefore the criteria were defined by RT events. This method was used to discriminate the noise events of which the pedestals behaved anomalously, which mostly originated from IHB signals, as illustrated in Fig. 12. Both TT and Ped cuts were independent on event energy. The third method was dependent on pulse shape discrimination (PSD), which was on the basis of correlations of A_{min}, A_{max}, Q, and T_{max}, since physical events performed distributions different in these parameters than those of noise events. The criteria were determined by physical events defined by AC^+ events of ^{137}Cs calibration data, as depicted in Fig. 13.

(2) AC^+ vs AC^- events selection (AC cut): Considering the χN interaction cross section, WIMPs can hardly induce signals in both pPCGe and NaI-AC detectors. However, a gamma ray can produce signals in both detectors. The distribution of Δt is presented in Fig. 14. The AC^+ events with the coincidence of pPCGe and NaI-AC are distributed in the specific band, while AC^- and RT events have a fixed Δt except for events with accidental coincidence. The accidental coincidence events are uniformly distributed in the time range. The trigger timing is defined by a constant amplitude discriminator of the S_{p6} signal, such that Δt between the two detectors varies with energy.

(3) Bulk vs surface events selection (BS cut): These selection criteria were the final cut to identify AC^- physical events which took place in the active bulk volume based on τ defined in Sec. IV.A. The scatter plot of τ vs energy of AC- events is shown in Fig. 15(a) and emerges two characteristic bands representing bulk (B) and surface (S) events, respectively. Typical B and S events as well as their fitting profile at the analysis energy threshold (∼500 eVee) are depicted in Fig. 15(b).

C. Efficiency evaluation

At a total DAQ rate of ∼3 Hz, the DAQ live time was 99.9% measured by the survival probabilities of the RT events generated by a pulse generator at high precision and stability. Different methods have been adopted to calibrate the efficiencies for different data selection criteria. The signal efficiencies for TT, Ped, and AC cuts, which are energy

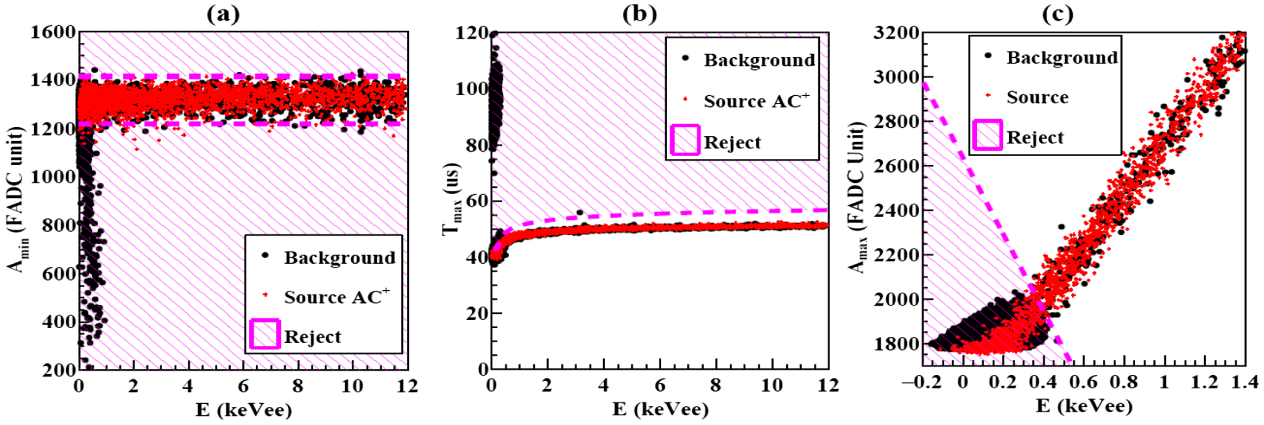

FIG. 13. The energy-dependent PSD cuts: (a) A_{min} cut, (b) A_{max}-T_{max} correlation cut, and (c) A_{max}-Q correlation cut.

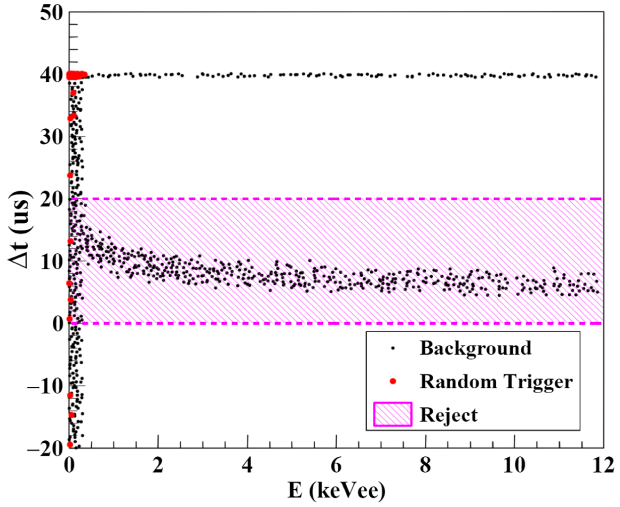

FIG. 14. Δt vs energy distribution and AC cut criteria. The rejected bands are the AC^+ events.

independent, can be evaluated by RT events accurately and were 94.0%, 96.8%, and nearly 100%, respectively.

The efficiency for the energy-dependent PSD cuts was derived from the physics events due to radioactive sources.

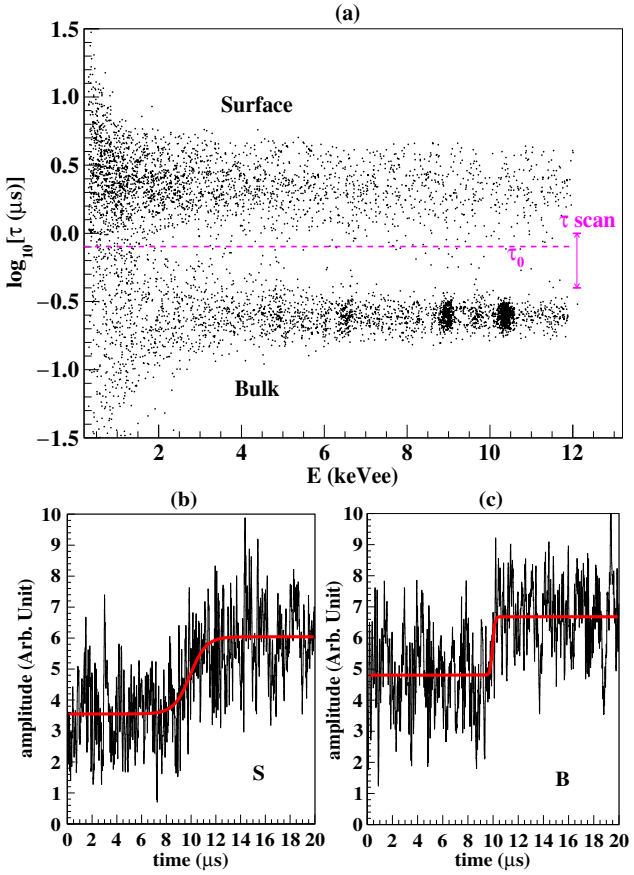

FIG. 15. (a) Scatter plot of $\log_{10}(\tau)$ vs energy for AC^- events; the BS cut criteria were defined by the τ_0 line. (b) and (c) Typical S and B events with energy at 500 eVee, together with their fitting profiles.

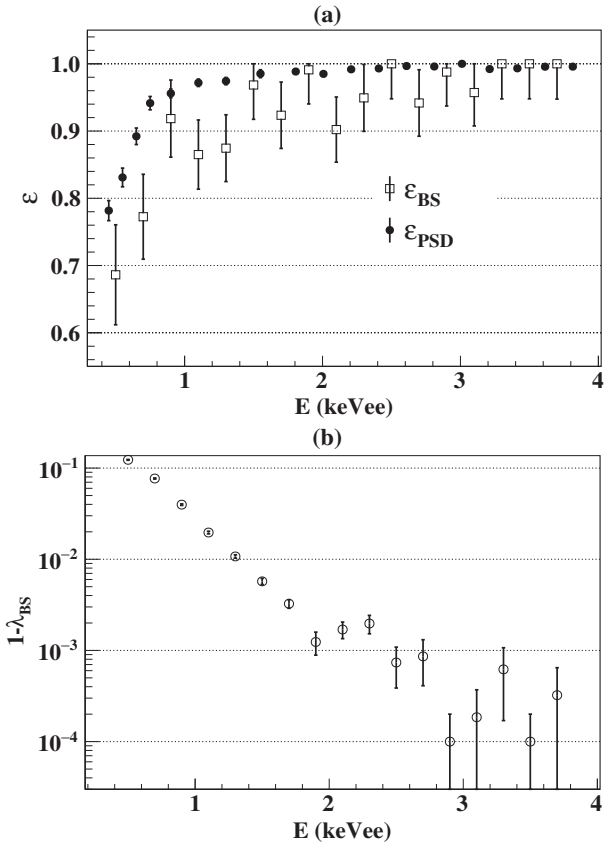

FIG. 16. (a) The measured ε_{PSD} and ε_{BS} with a 1σ statistic uncertainty as a function of energy. (b) The measured leakage ($1-\lambda_{BS}$) with a 1σ statistic uncertainty as a function of energy.

Exact cuts were applied to these samples, and the survival fractions provided measurements of ε_{PSD} , as displayed in Fig. 16(a).

The final efficiency calibration is for the BS cut, which required the evaluation of the B-signal retaining (ε_{BS}) and S-background rejection (λ_{BS}) efficiencies. These two efficiency factors can translate the measured spectra (B, S) to the actual spectra (B_0, S_0), and their relationship is illustrated by the following coupled equations:

$$\begin{aligned} B &= \varepsilon_{BS} \cdot B_0 + (1-\lambda_{BS}) \cdot S_0 \\ S &= (1-\varepsilon_{BS}) \cdot B_0 + \lambda_{BS} \cdot S_0. \end{aligned} \quad (1)$$

Since >99% of background from external radioactivity measured by our *p*PCGe detector is with energy less than 1.5 MeV [10], γ sources of corresponding energies [^{241}Am (59.5 keV), ^{57}Co (122 keV), ^{137}Cs (662 keV), and ^{60}Co (1173 keV, 1332 keV)] were used to calibrate the (ε_{BS}, λ_{BS}), and the detailed procedures were described in our previous work [12,20,24]. The energy-dependent ε_{BS} was shown in Fig. 16(a) and $1-\lambda_{BS}$ in Fig. 16(b). The (ε_{BS}, λ_{BS})-corrected spectra B_0 of the AC^- events ($AC^- \otimes B_0$) can be derived via Eq. (1):

$$B_0 = \frac{\lambda_{BS}}{\varepsilon_{BS}+\lambda_{BS}-1}\cdot B - \frac{1-\lambda_{BS}}{\varepsilon_{BS}+\lambda_{BS}-1}\cdot S$$
$$S_0 = \frac{\varepsilon_{BS}}{\varepsilon_{BS}+\lambda_{BS}-1}\cdot S - \frac{1-\varepsilon_{BS}}{\varepsilon_{BS}+\lambda_{BS}-1}\cdot B. \quad (2)$$

It was demonstrated that the neglected (that is, taking $\lambda_{BS}=1$) or underestimated S contaminations to the B samples can result in incorrectly assigned signal events.

D. Systematic uncertainties

The systematic uncertainties of $AC^- \otimes B_0$ derived from raw data are summarized in Table I, using two typical energy ranges for illustration. The systematic contributions arise from:

(1) Data taking:
   (a) The DAQ was in stable operation at more than 98% of the time. The trigger rate was low, and the DAQ live time was close to 100%. Contributions to systematic uncertainties were negligible.
   (b) Trigger efficiency: Since the analysis threshold (475 eVee) was much higher than the trigger threshold (246 eVee at 50%), the trigger efficiency of the physics events relevant to this analysis was 100%, resulting in a negligible contribution to the systematic uncertainties.
   (c) Fiducial mass: The error of the measured thickness of the dead layer gave rise to a 1% uncertainty at the fiducial mass. This corresponded to an additional 0.1% contribution to the total systematic uncertainty of the $AC^- \otimes B_0$ at 475 eVee.

(2) Signal selection: The systematic uncertainties originated from the stability of BC and AC cuts and were studied with the change of cut parameters around the nominal values. The BC cut contributed an additional 0.5% to contribution to the total systematic uncertainty at 475 eVee, while the contribution arising from the AC cut was negligible.

(3) Bulk events selection: The evaluation of systematic effects follow the procedures described in our earlier work [12,24]. In particular:
   (a) The leading systematic uncertainties are from the B-event selection and $(\varepsilon_{BS}, \lambda_{BS})$ calibration due to possible differences in locations and energy spectra between the calibration sources and background events. The calibration sources probed the surface effects due to both low-energy (surface richer) and high-energy (bulk richer) photons. The τ distributions for B events were identical for both sources and physics backgrounds, while those for S events showed an intrinsic difference due to the difference in surface penetration which manifest as the difference of slopes in the $(\varepsilon_{BS}, \lambda_{BS})$ plane [12]. The systematic uncertainties are derived from the spread of the $(\varepsilon_{BS}, \lambda_{BS})$ intersections of the calibration bands, relative to the combined best-fit solution. This leads to a 25.0% contribution to

TABLE I. The various contributions to the total error of $AC^- \otimes B_0$ at threshold and at a typical high-energy bin.

Energy bin	0.475–0.575 keVee	1.975–2.075 keVee
$AC^- \otimes B_0$ and errors ($kg^{-1}\,keV^{-1}\,day^{-1}$)	$4.00 \pm 0.64[stat] \pm 0.87[sys] = 4.00 \pm 1.08$	$3.61 \pm 0.36[stat] \pm 0.28[sys] = 3.61 \pm 0.46$
(I) Statistical uncertainties:		
(i) Uncertainties on calibration $(\varepsilon_{BS}, \lambda_{BS})$:	0.32	0.08
(ii) Derivation of $(\varepsilon_{BS}, \lambda_{BS})$-corrected bulk rates:	0.55	0.35
Combined:	0.64	0.36
(II) Systematic uncertainties:		
A. Data taking:		
(i) DAQ:	0.00	0.00
(ii) Trigger efficiency:	0.00	0.00
(iii) Fiducial mass:	0.05	0.05
B. Signal selection:		
(i) BC cuts:	0.08	0.05
(ii) AC cut:	0.00	0.00
C. Bulk event selection:		
(i) Rise-time cut value τ_0	0.27	0.12
(ii) Normalization range (3–5 keVee)	0.07	0.01
(iii) $(B_0, S_0) = (B, S)$ at normalization	0.10	0.10
(iv) Choice of discard region	0.30	0.06
(v) Source location	0.28	0.19
(vi) Source energy range and spectra	0.72	0.12
Combined:	0.87	0.28

the total error in the efficiencies-corrected bulk rates B_0, accounting for the most significant part of the total systematic uncertainty.

(b) The systematic uncertainties related with different locations were studied with the sources placed at several positions of the top and the side (the cylindrical surface) of the *p*PCGe. Among them, the ^{241}Am γ from the side were strongly attenuated due to additional thickness from the cylindrical copper support structure and curved surface of the germanium crystal and therefore did not produce useful signals. The higher energy γ from ^{57}Co, ^{137}Cs, and ^{60}Co at the top and side, as well as that from physics samples (BC $\otimes$ AC$^+$ and BC $\otimes$ AC$^-$), showed similar distributions in τ, independent of locations. The shift in (ε_{BS}, λ_{BS}) based on calibration source data at different locations was less than 4%, corresponding to a 3.7% contribution to the total error in the efficiencies-corrected bulk rates B_0.

(4) Choice of quenching function: Two studies were performed to investigate the sensitivities to exclusion limits from the choice of QF: (i) As displayed in Fig. 7, the red line evaluated by the TRIM software together with the yellow band (10% systematic uncertainty) were adopted. The analysis was performed by scanning the QFs within 10% of their nominal values. It was shown that the difference among these results was small; e.g., the variation of $\sigma^{SI}_{\chi N}$ was about 15% at $m_\chi = 8$ GeV/c^2, and the least stringent bounds among them at a given WIMP mass were adopted as our final physics limits. (ii) This was same procedure described in i, but the QFs evaluated by Lindhard ($k = 0.157$) and CoGeNT [13] were applied. It was concluded that the difference was small, e.g., about 14% deviations in $\sigma^{SI}_{\chi N}$ at $m_\chi = 8$ GeV/c^2). The results have been displayed in Ref. [12], and our formulation with TRIM provided the most conservative limits among the alternatives.

In our previous work, the 53.9 kg-days exposure has shown that the statistical uncertainties were dominant and contributed 86% relative to the total uncertainty [12]. As the exposure expanded to 335.6 kg-days, the statistical uncertainties were secondary, and systematic uncertainties dominated 81% relative to the total uncertainty. It was crucial to develop a new method to evaluate the (ε_{BS}, λ_{BS}) to decrease the systematic uncertainty further which contributes the main part of the uncertainty.

V. LIMITS ON WIMPS

The measured energy spectra and its evolution with the data selection progress are depicted in Fig. 17(a). Six cosmogenic nuclides can be identified clearly through the K-shell x-rays peaks, and the contributions of the corresponding L-shell x rays at the low-energy range can be calculated accurately since the ratios of the intensities of K-shell and L-shell x rays are definite, as shown in Fig. 18(a). The half-lives of the dominant nuclides can be measured by their K-shell x rays. Figure 17(b) displays the decay of ^{68}Ge, ^{65}Zn, and ^{55}Fe.

Ambient radioactivity external to the shielding structure was greatly suppressed and contributed to $\ll 10^{-6}$ kg^{-1} keV^{-1} day^{-1} to the low-energy background. Based on simulations [29], the measured events were due to high-energy gamma rays which produced a flat electron-recoil background in the low-energy region. The radioactivity was expected to originate from residual ^{238}U, ^{232}Th, and ^{40}K activity in the radon gas or the experimental hardware inside the shielding in the vicinity of the *p*PCGe detector. Quantitative studies of their locations and relative contributions are beyond the scope of this work and constitute our current research efforts. However, the analysis approach and software procedures used in the present work are independent of these details.

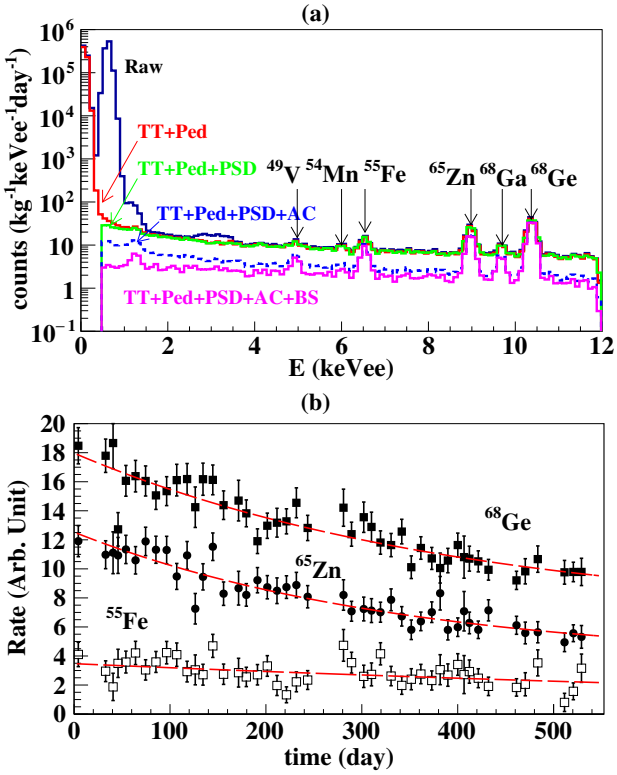

FIG. 17. (a) Measured energy spectra of the 1 kg-*p*PCGe detector and its evolution with the data selection progress. Six cosmogenic nuclides have been identified. (b) Time evolution of the three dominant K-shell x rays: ^{68}Ge, ^{65}Zn, and ^{55}Fe. The measured half-lives 279.7 ± 17.8, 235.3 ± 16.0, and 955.5 ± 411.2 days, respectively, are consistent with the nominal values of 270.8, 244.3, and 997.1 days.

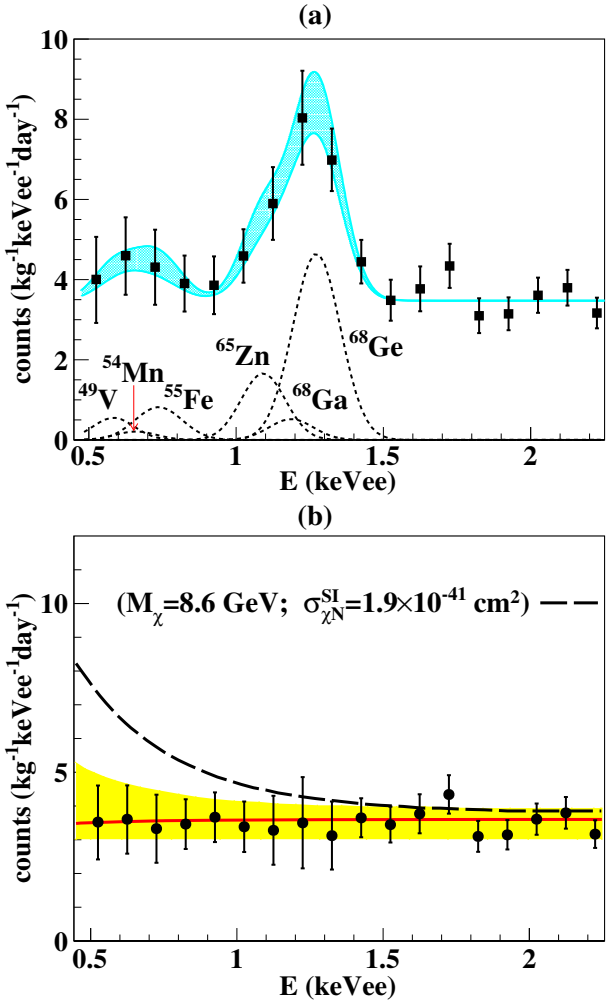

FIG. 18. (a) Energy spectrum with all selection cuts and efficiency correction factors applied. Various L-shell x rays are identified based on measured K-shell x rays intensities. The blue shaded region displays the total contribution of the L-shell x rays with a 1σ uncertainty band and superimposed on a flat background from ambient high-energy gamma rays. (b) The residual spectrum with contributions subtracted.The red line represents the best fit with two parameters: flat gamma background and spin-independent χ-N cross section, at $m_\chi = 8$ GeV/c^2, together with a 2σ uncertainty band. An excluded (m_χ; $\sigma^{SI}_{\chi N}$) scenario of CDMS(Si) [28] is superimposed.

The nature of the interaction between WIMPs with baryonic matter was *a priori* unknown. The data were analyzed with two benchmark χ-N cross sections: spin-independent (SI, scalar) and spin-dependent (SD, axial-vector) couplings:

$$\frac{d\sigma_{\chi N}}{dE_R} = \left(\frac{d\sigma_{\chi N}}{dE_R}\right)_{SI} + \left(\frac{d\sigma_{\chi N}}{dE_R}\right)_{SD}. \quad (3)$$

In general, the SI cross section can be written as

$$\left(\frac{d\sigma_{\chi N}}{dE_R}\right)_{SI} = \frac{2m_N}{\pi v^2}[Zf_p + (A-Z)f_n]^2 F^2(E_R), \quad (4)$$

where the $f_{p,n}$ describe the WIMP couplings to a proton and neutron. In most cases, $f_p \approx f_n$, and the Eq. (4) can be simplified to

$$\left(\frac{d\sigma_{\chi N}}{dE_R}\right)_{SI} = \frac{2m_N}{\pi v^2} A^2 (f_p)^2 F^2(E_R), \quad (5)$$

leading to the A^2 dependence of the SI cross section. The SD differential cross section can be expressed as

$$\left(\frac{d\sigma_{\chi N}}{dE_R}\right)_{SD} = \frac{16m_N}{\pi v^2}\Lambda^2 G_F^2 J(J+1)\frac{S(E_R)}{S(0)}, \quad (6)$$

where the J is the total angular momentum of the nucleus. Equation (6) illustrates that the SD cross section was proportional to a function of the total angular momentum of the nucleus, $J/(J+1)$ [30].

A best-fit analysis was applied to the residual spectrum of Fig. 17(b) after subtraction of the L-shell x rays, with two parameters representing the flat gamma background and possible χN spin-independent cross section $\sigma^{SI}_{\chi N}$, scanning m_χ between 4 and 30 GeV/c^2. The standard WIMP halo assumption [31] and conventional astrophysical models [32] were applied to describe WIMP-induced interactions, with the local WIMP density of 0.3 GeV/cm^3, the Maxwellian velocity distribution with $v_0 = 220$ km/s, and the galactic escape velocity of $v_{esc} = 544$ km/s. Exclusion plots on (m_χ, $\sigma^{SI}_{\chi N}$) at 90% confidence level are shown in Fig. 19(a), together with bounds and allowed regions from several representative experiments [13,23,28,33–36]. The sensitivity of $\sigma^{SI}_{\chi N}$ has been improved by a factor of 2 better at 8 GeV/c^2 over our work last year [12] due to several times larger exposure. Most of the light WIMP regions within 6 and 20 GeV/c^2 implied by earlier experiments were probed and rejected.

The limits on spin-dependent χ-neutron (denoted by χn) cross sections were also extracted. Exclusion plots on the (m_χ, $\sigma^{SD}_{\chi n}$) plane at 90% confidence level for light WIMPs were also derived, as depicted in Fig. 19(b), and bounds from other benchmark experiments [37–39] are also superimposed. The limits were derived from the model-independent approaches prescribed in Refs. [40,41]. Different ^{73}Ge nuclear physics matrix elements [42] adopted as input generated consistent results. The DAMA allowed region at low-m_χ was probed and excluded. Furthermore, it was shown that these results were competitive around $m_\chi = 6$ GeV/c^2. For completeness, the exclusion limits for the spin-dependent cross section derived from our earlier CDEX-0 data [8] are also displayed in Fig. 19(b).

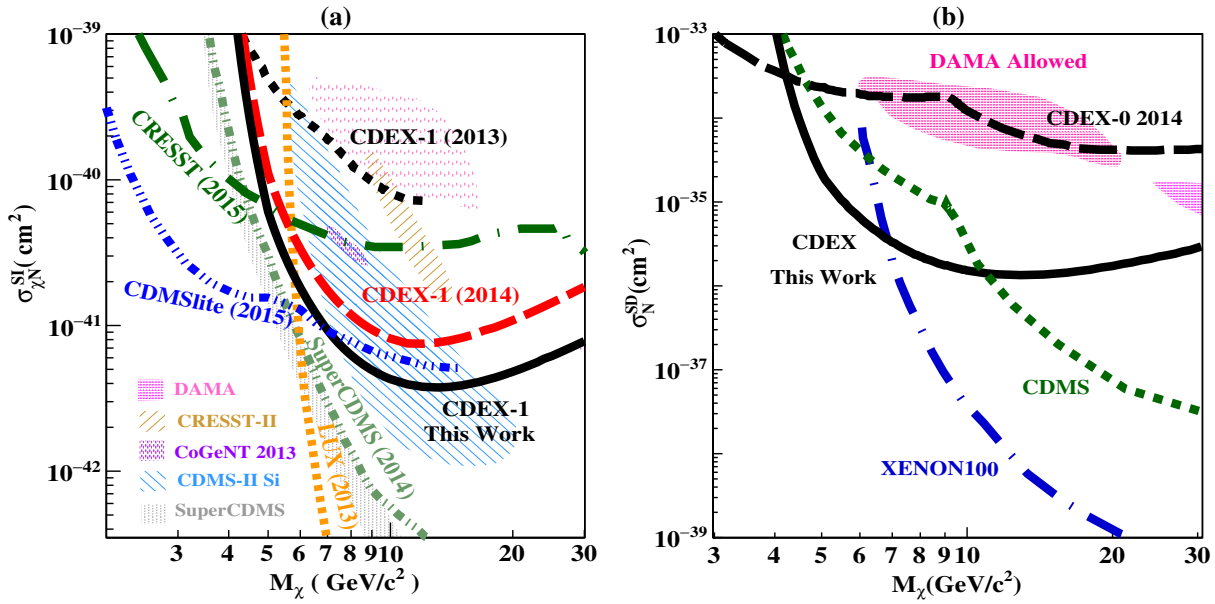

FIG. 19. The 90% confidence level upper limit of (a) spin-independent χ-N coupling and (b) spin-dependent χ-neutron cross sections. The CDEX-1 results from this work are depicted in solid black. Bounds from other benchmark experiments [10,12,13,23,28,33–36] are superimposed.

VI. SUMMARY AND PROSPECTS

The hardware, operation, and analysis details of the CDEX-1 experiment are described in this article. New limits on both SI and SD cross sections are derived with a data size of 335.6 kg-days, spanning over 17 months. The studies of annual modulation effects with this data set are being pursued. Another 1 kg *p*PCGe with a lower threshold is taking data at CJPL with data analysis and background understanding underway.

A *p*PCGe "CDEX-10" detector array with a target mass of the range of 10 kg and installed in liquid nitrogen as a cryogenic medium is being commissioned. A future option of replacement with liquid argon to serve in addition as an anti-Compton detector is being explored. In the meantime, a *p*PCGe detector completely fabricated by the CDEX Collaboration with a Ge crystal provided by the industry is being constructed. This would allow complete control of the choice of materials which are crucial toward the future goal of ton-scale Ge detectors for dark matter and double-beta decay experiments.

ACKNOWLEDGMENTS

This work was supported by the National Natural Science Foundation of China (Contracts No. 10935005, No. 10945002, No. 11275107, No. 11175099, No. 11475099, and No. 11475117), National Basic Research Program of China (973 Program) (Contract No. 2010CB833006) and NSC Grant No. 99-2112-M-001-017-MY3, and an Academia Sinica Principal Investigator 2011-2015 grant from Taiwan.

[1] K. J. Kang *et al.*, Front. Phys. **8**, 412 (2013).
[2] K. J. Kang, J. P. Cheng, Y. H. Chen, Y. J. Li, M. B. Shen, S. Y. Wu, and Q. Yue, J. Phys. Conf. Ser. **203**, 012028 (2010).
[3] K. A.Olive *et al.*, Chin. Phys. C **38**, 090001 (2014).
[4] Marc Schumann, Eur. Phys. J. Web Conf. **96**, 01027 (2015).
[5] P. Cushman *et al.*, arXiv:1310.8327.
[6] A. S. Barabash, Phys. Procedia **74**, 416 (2015); A. S. Barabash, AIP Conf. Proc. **1686**, 020003 (2015).
[7] S. M. Bilenky and C. Giunti, Mod. Phys. Lett. A **27**, 1230015 (2012); S. R. Elliott, Mod. Phys. Lett. A **27**, 1230009 (2012).
[8] S. K. Liu *et al.*, Phys. Rev. D **90**, 032003 (2014).
[9] P. S. BarbeauP. S. Barbeau, J I Collar, and O Tench, J. Cosmol. Astropart. Phys. 09 (2007) 009.
[10] W. Zhao *et al.*, Phys. Rev. D **88**, 052004 (2013); K. J. Kang *et al.*, Chin. Phys. C **37**, 126002 (2013).
[11] H. B. Li *et al.*, Phys. Rev. Lett. **90**, 131802 (2003); H. T. Wong *et al.*, Phys. Rev. D **75**, 012001 (2007).
[12] Q. Yue *et al.*, Phys. Rev. D **90**, 091701(R) (2014).
[13] C. E. Aalseth *et al.*, Phys. Rev. D **88**, 012002 (2013); arXiv:1401.3295.
[14] Y. C. Wu *et al.*, Chin. Phys. C **37**, 086001 (2013).

[15] Q. Du *et al.* (to be published).
[16] Z. M. Zeng, H. Gong, Q. Yue, and J. M. Li, Nucl. Instrum. Methods Phys. Res., Sect. A **804**, 108 (2015).
[17] Z. Zeng *et al.*, J. Radioanal. Nucl. Chem. **301**, 443 (2014).
[18] L. Li *et al.*, Chin. Phys. C **35**, 282 (2011).
[19] P. Yang, Master Dissertation, University of NanKai, 2011.
[20] H. B. Li *et al.*, Phys. Rev. Lett. **110**, 261301 (2013).
[21] J. F. Ziegler, http://www.srim.org.
[22] J. Lindhard *et al.*, K. Dan. Vidensk. Selsk. Mat. Fys. Medd. **33**, 10 (1963).
[23] R. Agnese *et al.*, arXiv:1509.02448.
[24] H. B. Li *et al.*, Astropart. Phys. **56**, 1 (2014).
[25] H. Jiang *et al.*, arXiv:1601.04305.
[26] E. Aguayo *et al.*, Nucl. Instrum. Methods Phys. Res., Sect. A **701**, 176 (2013).
[27] S. T. Lin *et al.*, Phys. Rev. D **79**, 061101 (2009).
[28] R. Agnese *et al.*, Phys. Rev. Lett. **111**, 251301 (2013).
[29] J. Su *et al.*, Chin. Phys. C **39**, 036001 (2015).
[30] D. G. Cerdeno and A. M. Green, Part. Dark Matter Obs. Mod. Searches **17**, 347 (2010).
[31] F. Donato, N. Fornengo, and S. Scopel, Astropart. Phys. **9**, 247 (1998).
[32] M. Drees and G. Gerbier, Phys. Rev. D **88**, 012002 (2013) and references therein.
[33] R. Bernabei *et al.*, Eur. Phys. J. C **56**, 333 (2008); **67**, 39 (2010).
[34] G. Angloher *et al.*, Eur. Phys. J. C **72**, 1971 (2012); G. Angloher *et al.*, arXiv:1509.01515.
[35] D. S. Akerib *et al.*, Phys. Rev. Lett. **112**, 091303 (2014).
[36] R. Agnese *et al.*, Phys. Rev. Lett. **112**, 241302 (2014).
[37] C. Savage *et al.*, arXiv:0808.3607.
[38] Z. Ahmed *et al.*, Phys. Rev. Lett. **106**, 131302 (2011); Z. Ahmed *et al.*, Phys. Rev. Lett. **102**, 011301 (2009).
[39] E. Aprile *et al.*, arXiv:1301.6620.
[40] A. Bottino, F. Donato, G. Mignola, S. Scopel, P. Belli, and A. Incicchitti, Phys. Lett. B **402**, 113 (1997).
[41] D. R. Tovey, R. J. Gaitskell, P. Gondolo, Y. Ramachers, and L. Roszkowski, Phys. Lett. B **488**, 17 (2000).
[42] M. T. Ressell, M. B. Aufderheide, S. D. Bloom, K. Griest, G. J. Mathews, and D. A. Resler, Phys. Rev. D **48**, 5519 (1993); V. I. Dimitrov, J. Engel, and S. Pittel, Phys. Rev. D **51**, R291 (1995).